Overview of ASDEX Upgrade Results

A. Kallenbach J. Adamek[1], L. Aho-Mantila[2], S. Äkäslompolo[2], C. Angioni, C.V. Atanasiu[3], M. Balden, K. Behler, E. Belonohy, A. Bergmann, M. Bernert, R. Bilato, V. Bobkov, J. Boom, A. Bottino, F. Braun, M. Brüdgam, A. Buhler, A. Burckhart, A. Chankin, I.G.J. Classen[4], G. Conway, D.P. Coster, P. de Marné, R. D'Inca, R. Drube, R. Dux, T. Eich, N. Endstrasser, K. Engelhardt, B. Esposito[5], E. Fable, H.-U. Fahrbach, L. Fattorini[6], R. Fischer, A. Flaws, H. Fünfgelder, J.C. Fuchs, K. Gál[7], M. García Muñoz, B. Geiger, M. Gemisic Adamov, L. Giannone, C. Giroud[8], T. Görler, S. da Graca[6], H. Greuner, O. Gruber, A. Gude, S. Günter, G. Haas, A.H. Hakola[2], D. Hangan, T. Happel[9], T. Hauff, B. Heinemann, A. Herrmann, N. Hicks, J. Hobirk, H. Höhnle[10], M. Hölzl, C. Hopf, L. Horton[11], M. Huart, V. Igochine, C. Ionita[12], A. Janzer, F. Jenko, C.-P. Käsemann, S. Kálvin[7], O. Kardaun, M. Kaufmann, A. Kirk[8], H.-J.Klingshirn, M. Kocan, G. Kocsis[7], H. Kollotzek, C. Konz, R. Koslowski[13], K. Krieger, T. Kurki-Suonio[2], B. Kurzan, K. Lackner, P.T. Lang, P. Lauber, M. Laux, F. Leipold[14], F. Leuterer, A. Lohs, T. Lunt, A. Lyssoivan[15], H. Maier, C. Maggi, K. Mank, M.-E. Manso[5], M. Maraschek, P. Martin[16], M. Mayer, P.J. McCarthy[17], R. McDermott, H. Meister, L. Menchero, F. Meo[14], P. Merkel, R. Merkel, V. Mertens, F. Merz, A. Mlynek, F. Monaco, H.W. Müller, M. Münich, H. Murmann, G. Neu, R. Neu, B. Nold[10], J.-M. Noterdaeme, G. Pautasso, G. Pereverzev, Y. Podoba, F. Pompon, E. Poli, K. Polochiy, S. Potzel, M. Prechtl, M.J. Püschel, T. Pütterich, S.K. Rathgeber, G. Raupp, M. Reich, B. Reiter, T. Ribeiro, R. Riedl, V. Rohde, J. Roth, M. Rott, F. Ryter, W. Sandmann, J. Santos[6], K. Sassenberg[17], P. Sauter, A. Scarabosio, G. Schall, K. Schmid, P.A. Schneider, W. Schneider, G. Schramm, R. Schrittwieser[12], J. Schweinzer, B. Scott, M. Sempf, F. Serra[6], M. Sertoli, M. Siccinio, A. Sigalov, A. Silva[6], A.C.C. Sips[11], F. Sommer, A. Stäbler, J. Stober, B. Streibl, E. Strumberger, K. Sugiyama, W. Suttrop, G. Tardini, C. Tichmann, D. Told, W. Treutterer, L. Urso, P. Varela[6], J. Vincente[6], N. Vianello[16], T. Vierle, E. Viezzer, C. Vorpahl, D. Wagner, A. Weller, R. Wenninger, B. Wieland, C. Wigger, M. Willensdorfer[18], M. Wischmeier, E. Wolfrum, E. Würsching, D. Yadikin, Q. Yu, I. Zammuto, D. Zasche, T. Zehetbauer, Y. Zhang, M. Zilker, H. Zohm

Max-Planck-Institut für Plasmaphysik, EURATOM Association, Garching, GERMANY, [1] Institute of Plasma Physics, Praha, Czech Republic, [2] Asscociation EURATOM-Tekes, Helsinki, Finland, [3] Institute of Atomic Physics, EURATOM Association-MEdC, Romania, [4] FOM-Institute for Plasma Physics Rijnhuizen, EURATOM Association, TEC, Nieuwegein, The Netherlands, [5] C.R.E ENEA Frascati, EURATOM Association, CP 65, 00044 Frascati, (Rome), Italy , [6] CFN, EURATOM Association-IST Lisbon, Portugal, [7] KFKI, EURATOM Association-HAS, Budapest, Hungary, [8] EURATOM/CCFE Fusion Association, Culham Science Centre, UK, [9] Ciemat, Madrid, Spain, [10] Institut für Plasmaforschung, Universität Stuttgart, Germany, [11] EFDA-JET, Culham, United Kingdom, [12] University of Innsbruck, EURATOM Association-AW, Austria, [13] Forschungszentrum Jülich, Germany, [14] Riso, EURATOM Association-RIS, Roskilde, Denmark, [15] LPP-ERM/KMS, EURATOM Association-Belgian State, Brussels, Belgium, [16] Consorzio RFX, EURATOM Association-ENEA, Padova, Italy, [17] Physics Department, University College Cork, Association EURATOM-DCU, Ireland [18] IAP, TU Wien, EURATOM Association-AW, Austria,
e-mail: Arne.Kallenbach@ipp.mpg.de

Abstract The ASDEX Upgrade programme is directed towards physics input to critical elements of the ITER design and the preparation of ITER operation, as well as addressing physics issues for a future DEMO design. After the finalization of the tungsten coating of the plasma facing components, the re-availability of all flywheel-generators allowed high-power operation with up to 20 MW heating power at I_p up to 1.2 MA. Implementation of alternative ECRH schemes (140 GHz O2- and X3-mode) facilitated central heating above $n_e = 1.2 \cdot 10^{20}$ m^{-3} and low q_{95} operation at $B_t = 1.8$ T. Central O2-mode heating was successfully used in high P/R discharges with 20 MW total heating power and divertor load control

with nitrogen seeding. Improved energy confinement is obtained with nitrogen seeding both for type-I and type III ELMy conditions. The main contributor is increased plasma temperature, no significant changes of the density profile have been observed. This behaviour may be explained by higher pedestal temperatures caused by ion dilution in combination with a pressure limited pedestal and hollow nitrogen profiles. Core particle transport simulations with gyrokinetic calculations have been benchmarked by dedicated discharges using variations of the ECRH deposition location. The reaction of normalized electron density gradients to variations of temperature gradients and the T_e/T_i ratio could be well reproduced. Doppler reflectometry studies at the L-H transition allowed the disentanglement of the interplay between the oscillatory geodesic acoustic modes (GAMs), turbulent fluctuations and the mean equilibrium ExB flow in the edge negative E_r well region just inside the separatrix. Improved pedestal diagnostics revealed also a refined picture of the pedestal transport in the fully developed H-mode type-I ELM cycle. Impurity ion transport turned out to be neoclassical in between ELMs. Electron and energy transport remain anomalous, but exhibit different recovery time scales after an ELM. After recovery of the pre-ELM profiles, strong fluctuations develop in the gradients of n_e and T_e. The occurrence of the next ELM cannot be explained by the local current diffusion time scale, since this turns out to be too short. Fast ion losses induced by shear Alfvén eigenmodes have been investigated by time-resolved energy and pitch angle measurements. This allowed the separation of the convective and diffusive loss mechanisms.

1. Introduction and technical boundary conditions

ASDEX Upgrade is operated with full tungsten coated plasma facing components since its 2007 experimental campaign [1]. After initial campaigns demonstrated plasma operation with pure tungsten plasma facing components (PFCs) without wall conditioning, phases with boronization intervals of 4-6 weeks were run in order to reduce the intrinsic impurity content, in particular that of O and C [2]. The lower intrinsic impurity content was found to reduce tungsten sputtering rates and therefore to widen the operational range. This domain is partly restricted by the occurrence of central tungsten accumulation in combination with electron density profile peaking [3]. The coverage of tungsten by boron layers appears to be a short term effect (less than 2 experimental days) for the erosion dominated outer divertor and main chamber wall surfaces, as can be shown by comparison of tungsten fluxes and concentrations measured in boron-free and boronized discharges. After repair of the flywheel generator EZ4, which was damaged in April 2006, full power and energy supply became available again in October 2009. In fact, retaining some of the measures taken before for the better exploitation of the limited power supply, peak power and maximum energy for ASDEX Upgrade operation are increased now as compared to the values which were in place before the EZ4 damage. In particular for low ELM frequency conditions, operation with tungsten plasma facing components (PFCs) requires a few MW central heating to prevent central tungsten accumulation. The use of ICRF for this purpose was found to be limited due to strong tungsten

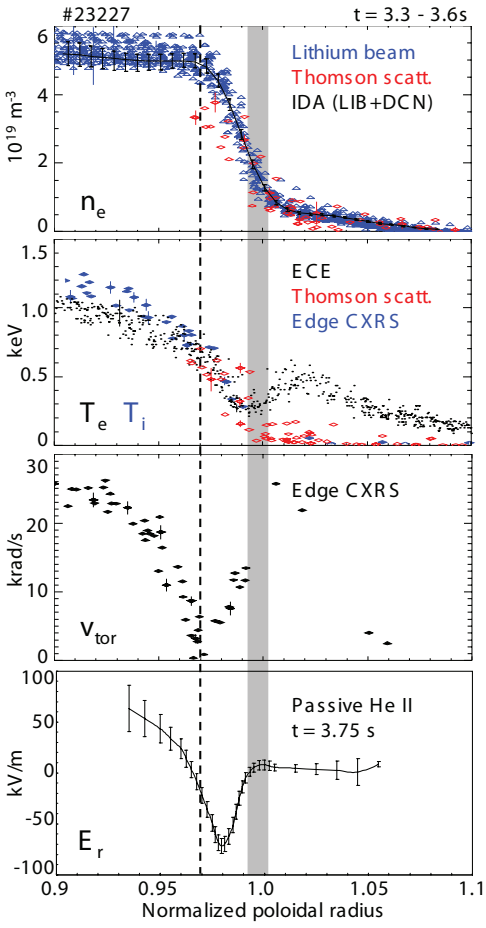

Figure 1: *Pedestal profiles of the electron density, electron and ion temperature, toroidal angular rotation frequency and radial electric field for the inter-ELM phase of a type-I ELMy H-mode.*

sputtering at the antenna limiters [4]. Improved antenna designs are currently under investigation. A first design change will be tested for one antenna in autumn 2010 [5]. Central ECRH with 140 GHz in the standard X2 scheme (B_t= -2.5 T) is restricted by the density cut-off, which occurs for peaked electron densities at 1 MA discharges and even for quite flat n_e profiles at higher currents. To allow for central heating at high currents and low q_{95} operation at reduced toroidal field, O2-mode heating (B_t= -2.5 T) and X3-mode heating (B_t= -1.8 T) have been developed [6]. Both schemes have a reduced single-pass absorption which potentially endangers in-vessel components due to ECR stray radiation. This problem has been solved by utilizing the X2 absorption on the high field side for the central X3 scheme. For the O2 scheme, a holographic reflector was installed at the inner wall which reflects the non-absorbed ECR radiation back through the plasma center and towards the robust passive stabilizing loop at the low field side. To protect the target tungsten coating from thermal overload in high power discharges, feedback-controlled nitrogen seeding has routinely been used for discharges with more than 10 MW of heating power. This paper summarises the experimental results obtained in ASDEX Upgrade during the autumn 2008 and 2009 campaign.

2. Pedestal physics

2.1. Inter-ELM structure of the pedestal The pedestal is the key area for the total stored energy as well as the impurity content of H-mode plasmas in AUG. While for the energy content temperature profile stiffness is the dominant mechanism which propagates pedestal parameters to the core plasma, the impurity content is determined by the interplay of edge impurity sources and the out-flushing of impurities from the pedestal by ELMs. Several

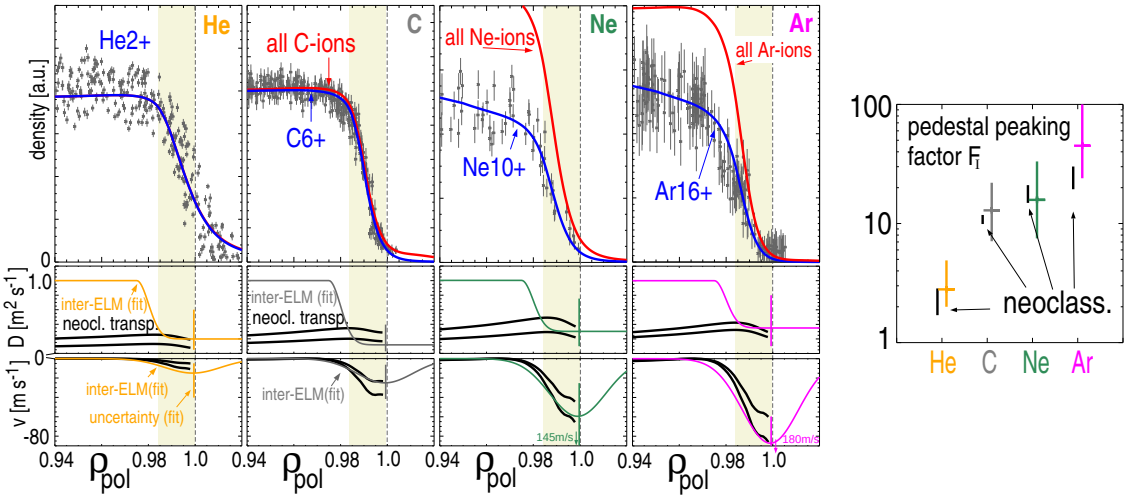

Figure 2: *Pedestal profiles of impurities with different charge Z measured by CXRS and STRAHL modelling of the corresponding transport coefficients D,v. Neoclassical values are shown for comparison. The right figure shows the experimental ETB impurity peaking factor versus the neoclassical predictions for the different species.*

diagnostics improvements allowed us to refine the picture of the spatial pedestal structure and its temporal evolution during an ELM cycle [7]. ELM-synchronized spatial profiles of various parameters during the inter-ELM phase are shown in figure 1 [8]. Only data which lie in the time window of -3.5 to -0.5 ms before an ELM are chosen, a radial shift of the plasma by 2.5 cm was employed to improve the spatial resolution. The most remarkable features are a negative peak of the toroidal rotation profile situated at the location of the density pedestal top as well as a pronounced negative dip of the radial electric field profile situated in the steep gradient zone. The E_r profile shown in figure 1 has been derived from the

(mainly poloidal) Doppler shift of passive HeII emission from the plasma edge. Its magnitude and spatial position corresponds in good approximation to the $\nabla p/n$ term in the radial force balance of the deuterium ions [9]. It has to be noted here that the radial electric fields derived from Doppler reflectometry measurements [10] show the same spatial structure (width and position of minimum), but for certain H-mode conditions systematically lower values of E_r. A possible reason may be the fact that Doppler reflectometry needs some degree of turbulence for backscattering which might be too low in high performance H-modes. Generally, the measured E_r corresponds to a perpendicular velocity of the fuel ions, i.e. their ExB rotation velocity approximately cancels their diamagnetic drift velocity. This behaviour is compatible with predominantly neoclassical ion transport in the edge transport barrier (ETB) region.

2.2. Impurity transport in the edge transport barrier region Further evidence of neoclassical ion transport in the ETB region is obtained from the analysis of radial profiles of different impurity species in the edge transport barrier region measured by the edge charge exchange recombination diagnostic, as shown in figure 2 [11]. Diffusion coefficient D and convective (inward) velocity v were obtained by a fit of the time dependent profile changes during an ELM cycle with the impurity transport code STRAHL. Also shown are the ETB impurity peaking factors (relative rise of the impurity density from the separatrix up to the pedestal top). Quantitative agreement is found between the fitted transport coefficients and the neoclassical prediction, resulting in a pronounced impurity density rise between separatrix and pedestal top. Obviously, for high-Z impurities an additional, outward directed transport mechanism is required to avoid excessive core concentrations. ELM flushing has been identified as a corresponding mechanism in the standard H-mode [12]. Therefore, for conditions of low ELM frequency, a sufficient outward impurity ion transport has to be maintained.

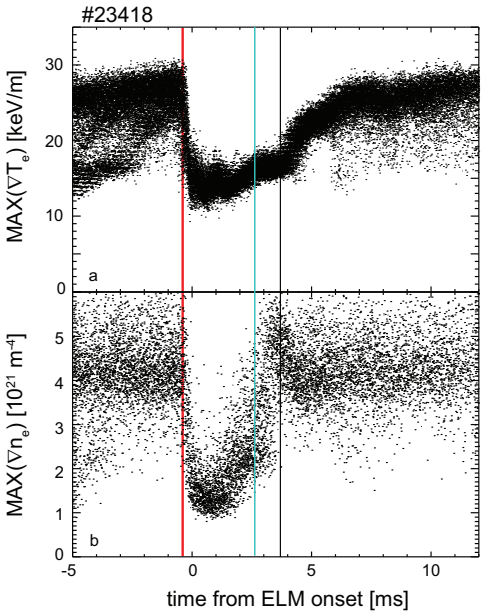

Figure 3: *Maximum gradients of the electron temperature and density during an ELM cycle, measured by ECE and combined Li-beam/interferometry, respectively. Data represent the coherent overlay of 105 ELM cycles.*

2.3. Transport variations during the ELM cycle The improved diagnostics also allowed the refinement of the picture of transport and stability of the pedestal region during an ELM cycle [7]. Figure 3 shows the temporal evolution of the maxima of the electron temperature and density gradients over an ELM cycle. The recovery of the gradients can be divided into different phases. After the ELM crash, first the T_e gradient recovers moderately. Then, it stays at a constant level while the density gradient rises. When the density gradient has recovered its pre-ELM value (or even a slightly higher value) about 4 ms after the crash, the T_e gradient accelerates its approach towards the pre-ELM value. When both gradients have approximately reached their final values about 7 ms after the crash, strong fluctuations of temperature and density gradients around their mean value set in, which may last for several ms. The occurence of the next ELM can vary within this fluctuating phase, which can lead to discharges having two distinct ELM frequencies, with the ELM occuring either right at the gradient recovery or several ms after the start of the fluctuating phase. The

empirical picture to explain this behaviour requires the interplay of different transport channels, the edge ballooning instability alone is not sufficient to explain the observed ELM behaviour. Peeling-ballooning theory suggests the edge current buildup time to be important for the temporal evolution of the ELM cycle, but our experimental findings suggest a more complicated picture. Current diffusion calculations showed that the edge current builds up almost as fast as the gradients, with a delay of less than 1 ms [7]. This disqualifies a delayed edge current as a trigger late during the fluctuating phase. The presence of ETG instabilities may explain why the T_e gradient does not increase during the density recovery phase. In the later phase, turbulent instabilities like filaments are supposed to be responsible for the large gradient fluctuations.

2.4. Interaction of turbulence and geodesic acoustic modes (GAMs) during the L-H transition The physics of the L-H transition is still not explained by first principle theory. Turbulence studies by means of Doppler reflectometry recently performed on ASDEX Upgrade [13] shed light on the possible role of geodesic acoustic modes (GAMs) on the formation of the edge transport barrier (ETB). The studies were performed under low density conditions, where the L-H threshold power increases with decreasing density. These conditions were favourable for the measurement of GAMs with Doppler reflectometry. A complicated interplay of GAMs, edge turbulence and mean flow shear could be disentangled. Figure 4a shows a time trace of the Doppler shift of fluctuations during a discharge phase close to an L-H transition, measured closely inside the separatrix around the position of the E_r minimum. The phases with enhanced Doppler shifts are associated with GAMs, the discharge is in an I-mode phase with confinement characteristics in between L-mode and H-mode. The improved confinement in the I-Phase is connected to a negative E_r well that is about a factor of 2 deeper than in the preceding L-mode. Synchronized Doppler spectra for the temporal phases with low and high turbulence levels are shown in figure 4b,c together with pure L and H-mode cases for comparison in 4d,e. These figures suggest the following picture for the interaction of turbulence, GAMs and equilibrium flows at the L-H transition, which is described in more detail in [13]. Strong turbulence excites GAM oscillations. These oscillations produce a sheared flow, which similar to a pronounced equilibrium flow stabilizes the turbulence and finally the GAM due to the loss of its driver. For these discharge conditions,

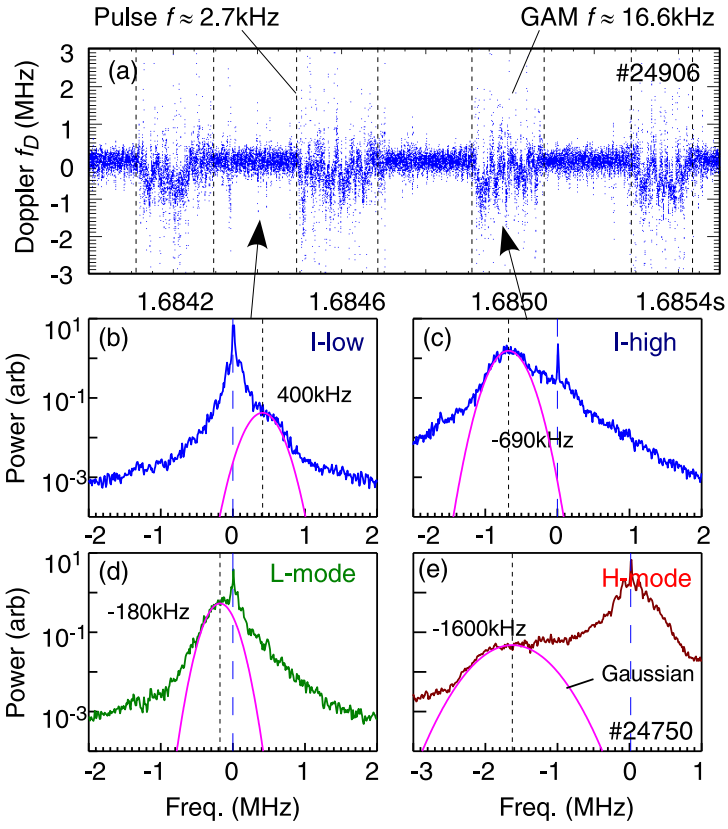

Figure 4: *Instantaneous Doppler shift f_D time series (a) showing several I-mode pulses with GAM oscillations present, plus synchronized Doppler spectra S(f) from the reduced (b) and enhanced (c) phases. For comparison are also shown an L-mode (d) earlier in the discharge and an H-mode spectrum (e) from similar # 24570 [13].*

several phases with low/high turbulence levels alternate. Finally, if the discharges enter into H-mode, the sheared equilibrium flow takes over in stabilizing the turbulence. At this point, no GAM is observed any more in the edge region. The intermittent turbulence stabilization may be the crucial ingredient for the transition into the fully developed H-mode. Although these results were obtained for low density conditions, it cannot be excluded that the described mechanism is also valid for any L to H transition.

3. Core transport

3.1. Core transport studies with ECRH Centrally deposited wave heating is an important tool to avoid accumulation of tungsten ions in the plasma center for standard, high current H-mode discharges in AUG [14]. To improve and to benchmark the theoretical understanding of core transport, dedicated transport studies were performed for different, low plasma current conditions [15]. These conditions allowed a strong variation of the T_e/T_i ratio and better experimental parameter characterisation as input for gyrokinetic calculations.

While for typical AUG parameters central heating leads to a flattening of the density profiles, a different behaviour can be obtained in lower I_p, low density conditions. Figure 5 shows the effect of central ECRH on various plasma profiles under such conditions [15]. Here, even though only 2MW of ECRH are added to a 5MW NBI heated discharge, a strong rise of the central electron temperature still occurs. The corresponding change in toroidal rotation is remarkable. The central rotation speed is drastically reduced and transport analyses show that diffusion alone can not explain the observed profiles; non-diffusive transport terms must be active. The central ion temperature is also considerably reduced as a consequence of the central electron heating. Similar to the electron density profile the boron density profile peaks moderately with centrally applied ECRH power. Variations of the ECRH deposition radius showed that the pronounced profile changes shown in figure 5 occur only for very central deposition. Theoretical studies [16] in fact explain the contrasting behaviour of different discharge types to central electron heating by the interplay of different control parameters like the T_e/T_i, normalized gradient lengths and collisionality in conditions of dominant ITG turbulence. Figure 6 compares measured normalized electron density inverse gradient lengths with quasi-linear and non-linear calculations for conditions corresponding to profiles shown in figure 5. Good agreement is found for the dependence on the T_e/T_i temperature ratio. In fact, the dependence of R/L_{ne} on all relevant experimental parameters (R/L_{Te}, R/L_{Ti}, collisionality) appears to be well ordered by the real frequency of the most unstable mode [17], see figure 6b. As shown in figure 6c, the change of the normalized gradient lengths of the boron densities is also satisfactorily predicted. The boron profiles are

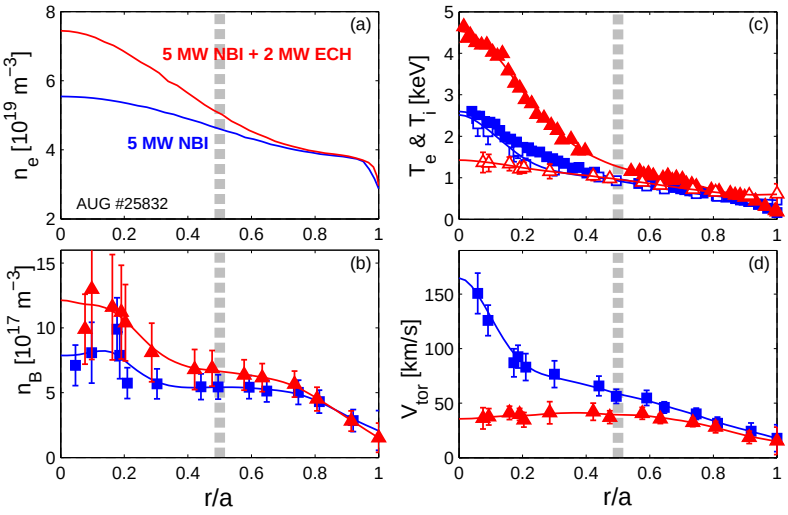

Figure 5: *Comparison of low density discharge phases with 5 MW NBI heating with and without 2 MW central ECRH at I_p= 0.6 MA. Shown are radial profiles of the electron density, T_i and T_e from CXRS and ECE diagnostics, the B^{5+} toroidal rotation and density profiles from CXRS.*

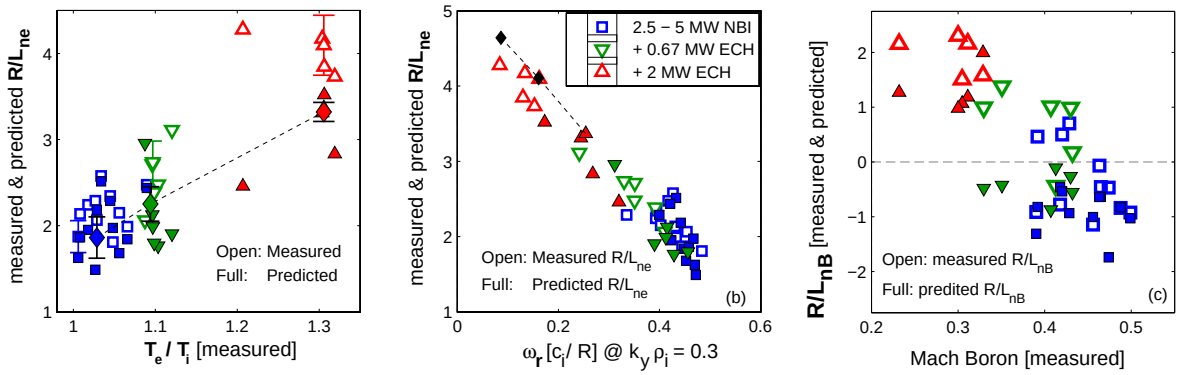

Figure 6: *Analysis of representative cases of the three heating phases corresponding to figure 5 at half radius. a) Comparison of predicted quasi-linear GS2 (full symbols with squares, triangles pointing down and up), nonlinear GYRO (diamonds connected by a dashed line) and measured (open symbols) values of R/L_{ne} as a function of the temperature ratio T_e/T_i. b) Real frequency of the most unstable mode at $k_y\rho_i = 0.3$. c) Normalized gradient length of B^{5+} ions vs. the toroidal Mach number [16].*

much less peaked compared to the electron density at half radius, or even slightly locally hollow. The toroidal rotation and its radial gradient [18] turned out to be an important ingredient for the turbulent boron ion transport, since positive ion density gradients (locally hollow profiles) are produced in the modelling only with the roto-diffusion included [16].

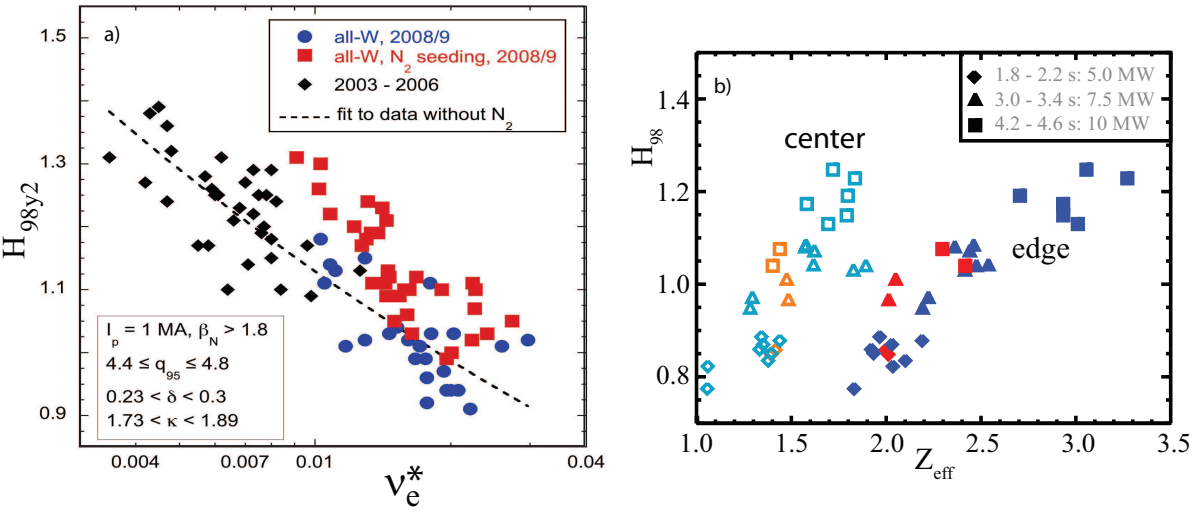

Figure 7: *a) $H_{98(y,2)}$ confinement factor vs. collisionality for different H-mode discharges with and without nitrogen seeding. b) H-factor $H_{98(y,2)}$ for discharges with /without (blue/red) nitrogen seeding versus Z_{eff} at ρ_{pol} = 0.2/0.9 (open/full symbols) [19].*

3.2. Effect of nitrogen seeding on plasma performance Feedback-controlled nitrogen seeding is used routinely in high power discharges to protect the divertor tungsten coatings from thermal overload [2]. As a positive side effect, improved energy confinement and an increased ELM frequency at shorter ELM duration have been observed [14]. The nitrogen puff leads mainly to increased divertor radiation, while the total radiation inside the separatrix stays approximately constant. The confinement improvement, as shown in figure 7a, is related to increased temperatures at the pedestal top and in the plasma core, while the electron density

profile is hardly effected by the presence of nitrogen. Analysis of Z_{eff} profiles derived from bremsstrahlung revealed a close correlation of the H_{98} confinement qualifier with Z_{eff} [19], as shown in figure 7b. These results suggest a simple, empirical picture for the confinement behaviour, based on the observation that impurity concentration profiles are hollow: Assuming that the total edge pressure is limited by an instability, the ion dilution by the presence of impurities results in a higher pedestal temperature. If the core temperature profile is stiff, which is a good approximation for AUG conditions, the increased pedestal temperature propagates to the plasma center. Hollow impurity profiles lead to a decrease of dilution towards the center and hence result in an increase of the total pressure and H_{98} caused by the higher ion density. In addition to the pedestal dilution effect, changes in core transport are expected. Gyrokinetic calculations suggest changes of the critical gradient as well as in the degree of temperature profile stiffness, both effects tend to cancel in their overall effect on confinement [20]. Clearly, further theory-based calculations are required for a quantitative understanding of the pedestal response to the nitrogen seeding.

3.3. Fast particle losses Fast particle transport through the plasma and their losses towards plasma facing components may affect the fusion rate, the current drive location and efficiency and the integrity of vessel structures in a fusion reactor. Various MHD modes may contribute to fast particle transport, like Alfvén cascades (ACs) and toroidal Alfvén eigenmodes (TAEs). Location and structure of the modes are determined by various diagnostics in ASDEX Upgrade, like soft X-ray diodes, reflectometry and fast ECE imaging measurements. Particle losses are detected by a fast ion loss detector (FILD). Figure 8 shows the raw signal and spectrograms obtained by the FILD detector during a discharge with AC and TAE activity [22]. The raw signal exhibits a fluctuating component, which is closely related to the frequency signatures of the MHD activities as observed by soft X-ray and Mirnov coils. This component of the fast ion losses is related to a convective loss mechanism, where the perturbing field amplitude leads to the direct loss of particles. Analysis with the HAGIS code revealed that the lost particles are not those which dominate the drive [23]. The FILD raw signal also exhibits a component which is time-independent on the MHD mode time scales (lower envelope in figure 8a). This component is attributed to a diffusive loss

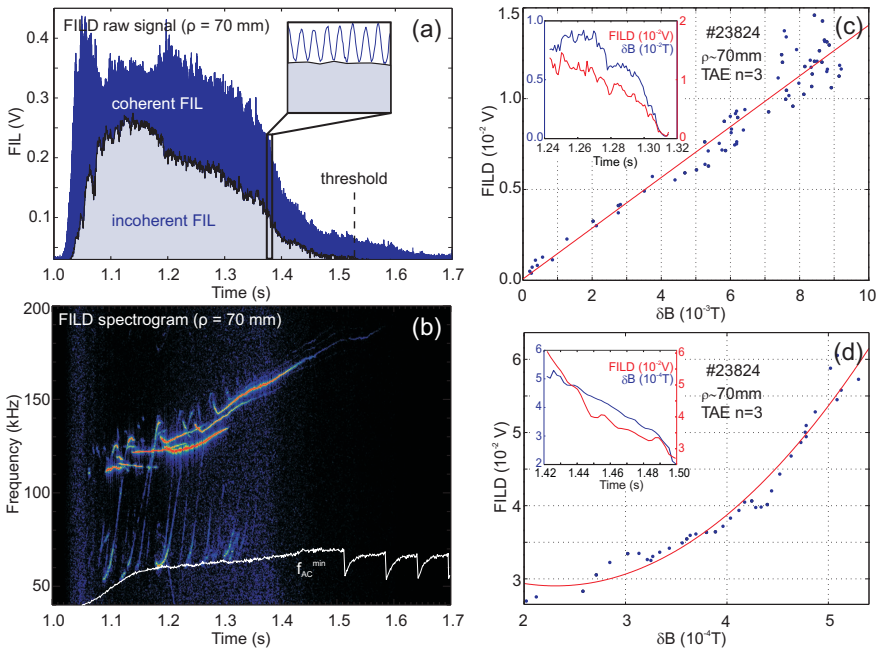

Figure 8: *a) Raw signal of the fast ion loss detector during a pulse with strong MHD activity. b) Spectrogram showing AC and TAE activity. The geodesic frequency f_{AC}^{min} [21] is indicated in white for reference. c) Linear dependence of coherent FIL signal on magnetic fluctuating amplitude δB interpreted as convective losses. d) Non-linear (offset-quadratic) dependence of incoherent FIL signal on δB interpreted as conductive losses.*

term, invoking more than one perturbation. The different behaviour of the convective and diffusive losses is shown in figure 8c,d, where a linear and a quadratic dependence on the perturbed field amplitude is found. Investigations of turbulent fast ion transport by means of fast ion D_α (FIDA) and collective Thomson scattering (CTS) diagnostics have started [22].

4. Power exhaust and plasma-wall interaction

4.1. High power exhaust experiments The ratio of separatrix power flux and major radius, P/R, is a performance parameter for divertor power exhaust and a measure for the effort required to keep the divertor peak power load below a certain critical level. High power experiments were conducted with feedback-controlled nitrogen seeding to keep the target peak heat flux at a moderate level. Figure 9 shows time traces of a discharge with 20 MW heating power, including about 1 MW central ECRH in O2 mode (central electron density is above X2 cut-off density). Good energy confinement ($H_{98(y,2)}$=1) could be obtained simultaneously with a low impurity content of the core plasma ($\overline{Z}_{eff} < 1.8$). The discharge used also strong deuterium puffing to enhance SOL/divertor radiation, the corresponding confinement degradation is compensated by the improvement caused by nitrogen. The radiation distribution from bolometer tomography is shown in the middle of figure 9, about half of the radiated power is emitted in the SOL and divertor. It is worthwhile to compare the measured divertor and SOL radiation of $\approx$ 6 MW with a simple analytical estimate based on a radiative loss model coupled to classical parallel electron heat conduction [24]. SOL and divertor are approximated as a single flux tube with the radial width equal to the power decay length λ_p in the outer midplane. Electron pressure conservation is assumed along the flux tube.

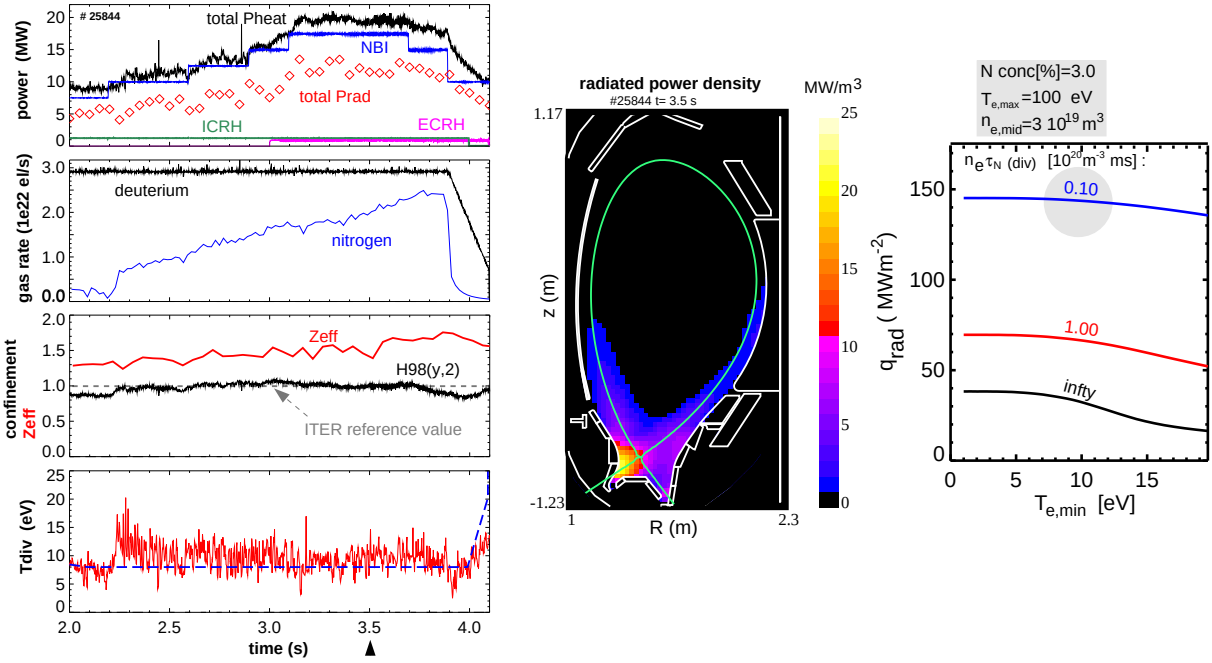

Figure 9: *High P/R discharge with divertor power load control by nitrogen seeding in ASDEX Upgrade. left: Time traces of various plasma parameters. The strong deuterium puff allows for low Z_{eff} in the core plasma, while the confinement improvement due to nitrogen maintains H-mode confinement with $H_{98,y2}$=1. Middle: radiation distribution from tomographic bolometer reconstruction at t=3.5 s. right: estimated maximum radiated parallel power flux density from simple analytical model and ADAS data. 'infty' refers to Coronal conditions, non-Coronal enhancement is expected for the present conditions (grey area) corresponding to $n_e\tau_N = 10^{16}\ m^{-3}s$.*

The radiated heat flux is calculated as the integral of the weighted radiative loss function, L_z, where non-Coronal effects are introduced via the parameter $n_{e,div}\tau_N$ [25]. With λ_p= 5 10^{-3} m about 5 MW radiated power is predicted for the conditions of the discharge shown in figure 9, well in line with the experiment. A factor of 4 enhancement above the Coronal radiation level is obtained for these conditions, a lower level of enhancement has to be assumed for reactor conditions with higher divertor density and longer residence time τ_N. Nitrogen seeding does not significantly enhance the radiation inside the pedestal. To control the power flux through the pedestal independently from the divertor heat flux, multi-species impurity seeding has to be applied. Initial experiments have been performed with combined N and Ar injection [26].

4.2. Tungsten melt experiment So far, tungsten erosion and transport studies concentrated on normal H-mode operation. For these conditions, the outer limiters have been identified as the tungsten source which is most important for the observed core tungsten concentration [12]. Despite the higher absolute W source strength in the divertor, its good W retention capability leads to a relatively small core penetration. For preparation of future high power devices with a tungsten divertor, melting events have to be studied, which can occur either during abnormal events or due to imperfections of tile alignments. To simulate an abnormal tungsten melting

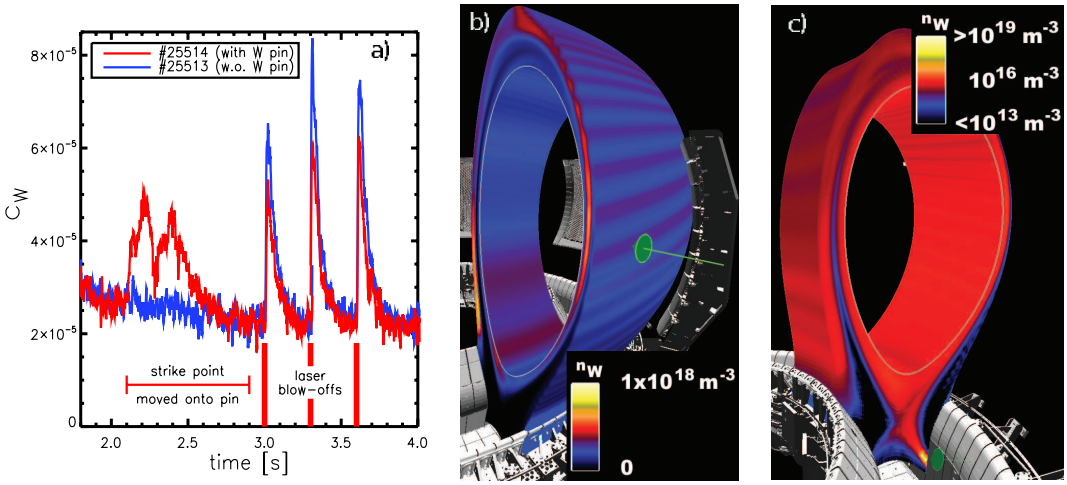

Figure 10: *W concentration measurements and EMC3-Eirene modelling of a W melt experiment. a) measured W concentration for W melting and W-LBO. b) EMC3-Eirene calculation of W injection in the midplane by laser blow-off. c) EMC3-Eirene calculation for ablation in the divertor at the strike point position (log scale) [27].*

in the divertor, small W pin probes were inserted into the divertor plasma by means of a manipulator for attached L-mode and detached H-mode conditions [28]. The experiments were performed under well diagnosed and stable plasma conditions, results are shown in figure 10. Main chamber injection of tungsten was done by laser blow-off (LBO) later in the discharge for the same plasma conditions, allowing the comparison of the rise of the core tungsten concentration for the different release locations. Thus, the divertor screening for molten W injection was measured. For the H-mode case, tungsten core penetration probabilities of 1/260 and 1/11 were derived for the divertor and the main chamber, respectively [27]. The experiments were accompanied by numerical simulations with the 3D edge code EMC3-Eirene. A high divertor screening could be reproduced, albeit a strong dependence of the penetration probability from the distance of the injection position to the strike point was found in the modelling.

4.3. Disruption mitigation Disruptions have been successfully mitigated with massive gas injection (MGI) [29] and disruption avoidance or delay by off-axis ECRH has been demon-

strated for high β_N discharges [30]. During MGI mitigated discharges, newly installed AXUV bolometer arrays allowed the study of fast radiation events including the VUV radiation, which is blocked by the filters of the soft X-ray diagnostic. The temporal and spatial evolution of the radiating zone is particularly important, since large asymmetries may lead to excessive wall loads in ITER. Figure 11 shows the propagation of the radiating zone during a fast plasma shutdown by massive gas injection, measured by poloidal fans of AXUV diodes in the sector of the gas valve and on the opposite side of the torus. A poloidal propagation of filamentary radiating layers is clearly observed. On the opposite side of the torus, the radiation rise is substantially delayed. Impurities are supposed to reach the HFS predominantly by streaming parallel to the field lines, plus some additional drift effect. The emissivity front moves towards the plasma center, does not penetrate that far, but reaches the surface with q$\approx$ 2 within 2 ms; afterwards the thermal quench sets in. The experiments with one MGI valve generally show a highly anisotropic radiating layer. To reduce this localization, the simultaneous use of several MGI valves may be required.

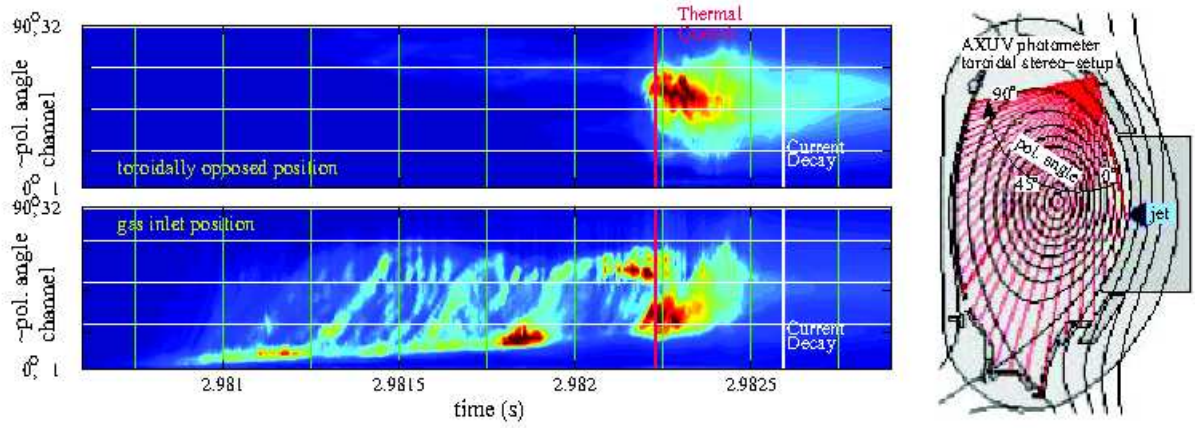

Figure 11: *Temporal and spatial development during a Ne-MGI mitigated disruption in a toroidal position opposite to the MGI valve and in sector of the MGI valve for # 24442 [29]. The right figure shows the geometry of the viewing lines, from this, a poloidal motion of filaments over the plasma top towards the high field side can be inferred in the gas valve sector.*

Disruption avoidance or at least substantial delay has been achieved by localized injection of 1.5 MW ECRH onto the q=2 resonant surface in a high β_N scenario [30]. Like the MGI, in standard $I_p \geq 1$ MA operation the ECRH is triggered by the locked mode monitor precursor signal of the 2/1 mode. For suitable scenarios, ECRH injection can be considered as a complementary technique to MGI for disruption control.

4.4. Plasma-wall interaction with nitrogen seeding Fuel retention and heat removal capabilities of tungsten depend strongly on its microscopic characteristics in the near-surface layers. A modification of the material properties is expected due to the storage of nitrogen. The formation of a W nitride layer with a 1:1 atomic ratio in the first few nm below the surface had been observed in laboratory experiments [31]. N particle balance in AUG seeded discharges revealed even an order of magnitude higher N storage of about 10^{21} N atoms/m^2. The higher storage is expected to be caused by surface roughness and co-deposition with B and C in local recessions in the W surface [25]. Laboratory studies showed a reduction of the W sputtering yield by N compared to a pure W surface. Figure 12 shows W sputtering yield measured in AUG for conditions of dominant sputtering by N. Within the considerable uncertainties, the measured yields agree with the TRIM predictions without a modification of the yields due to N storage.

5. Conclusions and outlook

Re-establishment of its full flywheel-generator capabilities allowed us to operate the full-tungsten ASDEX Upgrade tokamak with up to 20 MW heating power. New results have been obtained in particular on the pedestal structure and transport, the L-H transition, core transport, fast ion losses, high power operation with radiative cooling and plasma-wall interaction. After installation of the first set of 8 resonant magnetic perturbation (RMP) coils, AUG will resume plasma operation at the end of Oct 2010. Two new gyrotrons will increase the ECRH capability up to 5 MW. Characterisation of a modified ICRF antenna will be used to validate antenna models developed with HFSS and TOPICA codes, aiming towards an antenna design leading to reduced tungsten erosion. Power exhaust studies will aim at the integration of impurity seeding and RMP controlled ELMs in the tungsten PFC environment.

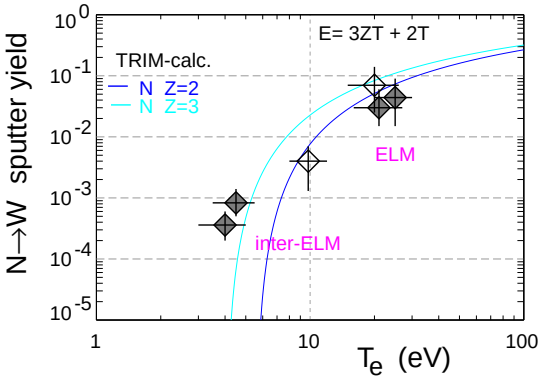

Figure 12: *Measured W sputtering yields for nitrogen seeded discharges versus an analytic fit of TRIM calculations for N^{2+} and N^{3+} ions. Solid symbols represent conditions close to N-saturated tungsten divertor surface. The open symbols are not N-saturated [25].*

References

[1] NEU, R. et al., Plasma Physics and Controlled Fusion **49** (2007) B59.
[2] KALLENBACH, A. et al., Nuclear Fusion **49** (2009) 045007.
[3] KALLENBACH, A. et al., Plasma Physics and Controlled Fusion **47** (2005) B207.
[4] BOBKOV, V. V. et al., Journal of Nuclear Materials **363-365** (2007) 122.
[5] NOTERDAEME, J.-M. et al., IAEA-CN-180/EXM/P7-21 .
[6] HÖHNLE, H. et al., IAEA-CN-180/P7-25 .
[7] BURCKHART, A. et al., Plasma Phys. Controlled Fusion (2010) 105010.
[8] KURZAN, B. et al., IAEA-CN-180/EXC/P3-03 .
[9] WOLFRUM, E. et al., Plasma Physics and Controlled Fusion **51** (2009) 124057 (9pp).
[10] CONWAY, G. D. et al., Plasma Physics and Controlled Fusion **46** (2004) 951.
[11] PÜTTERICH, T. et al., PSI 2010, I-14, to be published in Journal of Nuclear Materials .
[12] DUX, R. et al., IAEA-CN-180/EXD/6-2 .
[13] CONWAY, G. et al., IAEA-CN-180/EXC/7-1 .
[14] GRUBER, O. et al., Nuclear Fusion **49** (2009) 115014.
[15] MCDERMOTT, R. et al., submitted to Plasma Phys. Control. Fusion .
[16] ANGIONI, C. et al., submitted to Nuclear Fusion .
[17] FABLE, E. et al., Plasma Phys. Controlled Fusion **52** (2010) 015007.
[18] CAMENEN, Y. et al., Physics of Plasmas **16** (2009) 062501.
[19] RATHGEBER, S. K. et al., Plasma Physics and Controlled Fusion **52** (2010) 095008.
[20] SCHWEINZER, J. et al., IAEA-CN-180/EXC/P2-07 .
[21] BERK, H. et al., Physical Review Letters **87** (2001) 185002.
[22] GARCÍA-MUñOZ, M. et al., IAEA-CN-180/EXW/P7-7 .
[23] LAUBER, P. et al., IAEA-CN-180/THW/2-2Ra .
[24] LACKNER, K. et al., Fusion Eng. and Design **22** (1993) 107.
[25] KALLENBACH, A. et al., PSI 2010, J. Nucl. Mat. in press .
[26] NEU, R. et al., IAEA-CN-180/EXD/P3-24 .
[27] LUNT, T. et al., PSI 2010, to be published in Journal of Nuclear Materials .
[28] KRIEGER, K. et al., PSI 2010, to be published in Journal of Nuclear Materials .
[29] PAUTASSO, G. et al., IAEA-CN-180/P9-1 .
[30] ESPOSITO, B. et al., IAEA-CN-180/EXW/10-2Ra .
[31] SCHMID, K. et al., Nucl. Fusion **50** (2010) 025006.